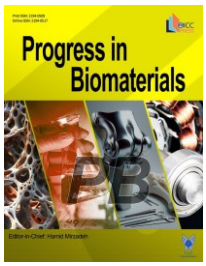

Volume 14, Issue 3, 2025: Article 12

Progress in Biomaterials (PIBM)

https://doi.org/10.57647/pibm-2025-17593

Encapsulation of IR783 in UiO-66 MOFs for Improved Photodynamic Efficacy Against Breast Cancer Cells

Sinem Şahinoğlu, Gülşah Şanlı-Mohamed*

Department of Chemistry, İzmir Institute of Technology, 35430, İzmir, Türkiye

***Corresponding author:** gulsahsanli@iyte.edu.tr

Original Research

Received:
04 May 2025

Revised:
12 August 2025

Accepted:
30 September 2025

Published in Issue:
30 September 2025

Abstract

Breast cancer remains the most prevalent malignancy among women worldwide, underscoring the need for innovative therapeutic strategies beyond conventional modalities. Photodynamic therapy (PDT) offers a non-invasive approach that leverages light-activated photosensitizers to induce reactive oxygen species (ROS)-mediated tumor cell death. IR783, a near-infrared fluorescent (NIRF) heptamethine cyanine dye, has shown promise as a theranostic agent in cancer therapy due to its tumor-selective uptake and pro-apoptotic effects. However, its clinical potential is hindered by poor stability, rapid dissociation in polar environments, low quantum yield, and suboptimal tumor accumulation. In this study, we developed a multifunctional nanoplatform by encapsulating IR783 into UiO-66, a zirconium-based metal-organic framework (MOF), to enhance the delivery and photodynamic performance of the dye (IR783@UiO-66). The system was structurally characterized, and its biocompatibility and drug release profiles were evaluated. In vitro experiments were conducted to assess the cytotoxic and phototoxic effects of IR783, UiO-66, and IR783@UiO-66 on breast cancer cell lines (MCF-7, MDA-MB-231) and normal breast epithelial cells (MCF-10A), under LED irradiation at varying light intensities (18–144 J/cm²) and exposure durations (7.5–60 min). The results demonstrated that IR783@UiO-66 significantly reduced cancer cell viability in a dose- and light-dependent manner while sparing normal cells. Free IR783 showed slightly higher phototoxicity, attributed to differences in release kinetics and loading efficiency. UiO-66 alone exhibited negligible cytotoxicity under irradiation, confirming its safety profile. This study highlights the potential of UiO-66 as a promising nanocarrier for enhancing IR783-mediated PDT, offering a synergistic strategy for targeted and efficient breast cancer therapy.

Keywords: Photodynamic therapy (PDT), Breast cancer, IR783, UiO-66, Metal-organic frameworks (MOFs)

Cite this article: Şahinoğlu, S., Gülşah Şanlı, M., (2025). Encapsulation of IR783 in UiO-66 MOFs for Improved Photodynamic Efficacy Against Breast Cancer Cells, *Progress in Biomaterials,* 14(03), Article 12.
https://doi.org/10.57647/pibm-2025-17593

Graphical abstract

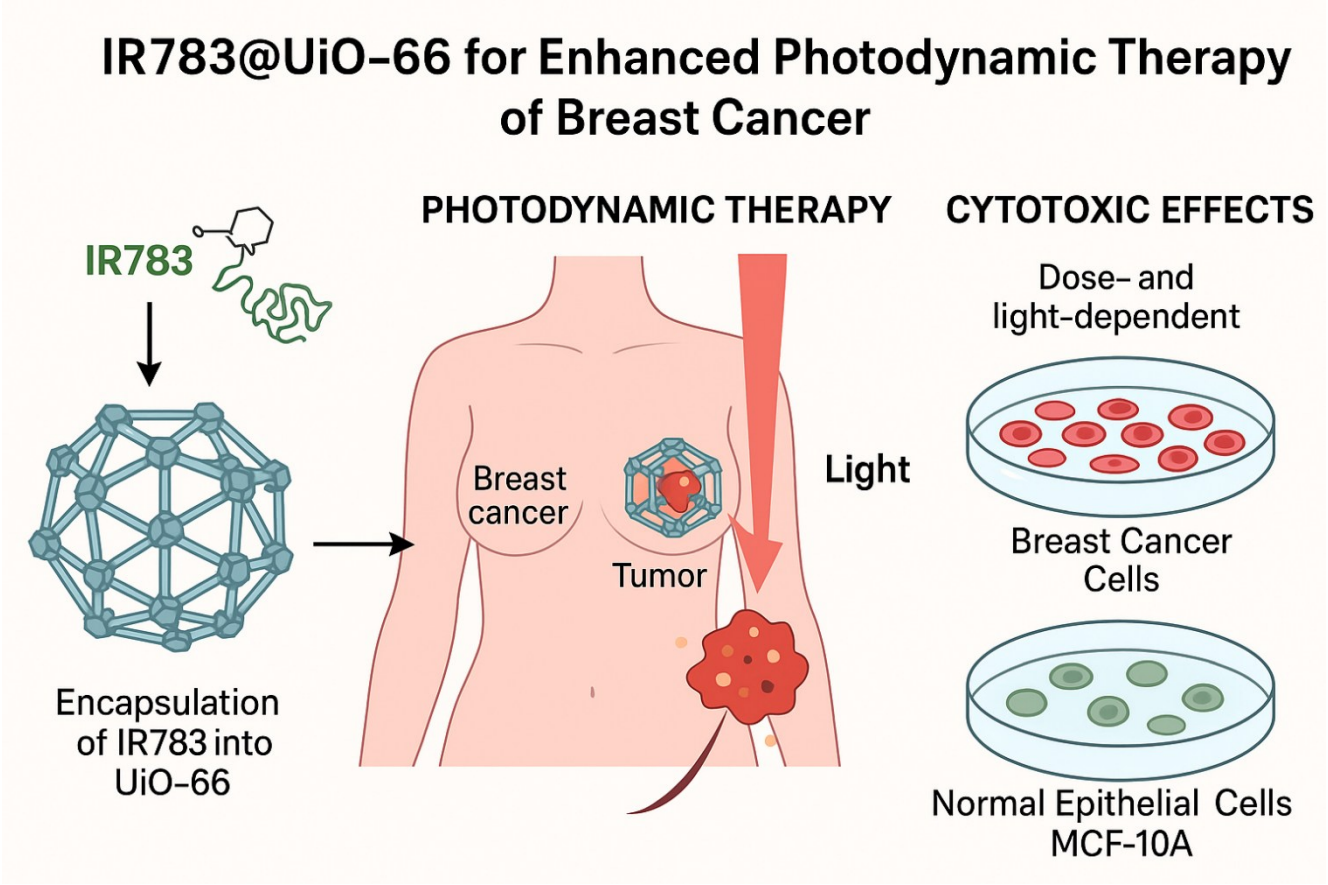

1. Introduction

Breast cancer remains the most frequently diagnosed malignancy among women worldwide, posing a significant global health challenge [1,2]. Although rare in men, it still accounts for approximately 1% of all breast cancer diagnoses [3,4]. According to the International Agency for Research on Cancer (IARC) GLOBOCAN, 2.6 million new cases of breast cancer were reported among women in 2020, making it the most commonly diagnosed cancer worldwide during that year [5]. The primary treatment modalities for breast cancer include radiation therapy, chemotherapy, surgical procedures (mastectomy or breast-conserving surgery), endocrine therapy, and targeted therapies [6,7]. Despite advancements, limitations in imaging and therapeutic effectiveness highlight the need for novel treatment strategies [8].

PDT has emerged as a potential alternative to conventional treatments, especially for patients who are not candidates for surgery [9,10]. PDT leverages the photochemical reaction between a specific wavelength of light and a systemically administered, non-toxic photosensitizer to generate singlet oxygen ($^1O_2$) and ROS, leading to localized cell death through necrosis or apoptosis [11,12]. The therapeutic efficacy of PDT is attributed to its direct cytotoxic effects on cancer cells, modulation of the immune response, and disruption of blood and lymphatic vessels [13,14]. However, PDT efficacy is highly dependent on the photosensitizer's ability to produce singlet oxygen efficiently [15].

Among the promising photosensitizers, NIRF heptamethine cyanine dyes, including IR783, have demonstrated significant potential as theranostic agents for antitumor PDT [16,17]. These dyes exhibit unique photophysical properties, including substantial Stokes shifts, which facilitate both imaging and therapeutic applications [18,19]. However, a fundamental challenge of PDT using these dyes is the limited tissue penetration of visible light, which restricts therapeutic efficacy to superficial lesions [20]. In this context, NIRF heptamethine cyanine dyes offer an advantage by minimizing background noise and autofluorescence, thereby enhancing imaging sensitivity and enabling deeper tissue penetration [19].

IR783, a NIRF heptamethine cyanine dye, has gained attention for its potential in cancer diagnosis and therapy. Notably, IR783 demonstrates selective uptake and

10.57647/pibm-2025-17593

accumulation in cancer cells while maintaining low toxicity in normal tissues [21]. It has been shown to target various tumors, including breast, brain, bladder, prostate, and colon cancers [8,22]. Moreover, IR783 is known to promote apoptosis in breast cancer cells by inducing mitochondrial fission, suggesting a role of mitochondria in inhibiting cancer cell proliferation and migration [23]. Nevertheless, clinical application of IR783 in PDT is limited due to challenges such as low tumor accumulation and poor light penetration [24,25] . To overcome these challenges, various nanocarrier-based delivery systems have been developed to enhance the accumulation and retention of photosensitizers in tumors [25,26]. Notably, no study to date has reported the incorporation of IR783 into MOF, despite their favorable characteristics for such applications.

MOFs are a class of hybrid materials formed by the coordination of metal ions or clusters with organic ligands, resulting in highly porous, crystalline architectures [27]. Their high surface area, tunable pore size, and excellent drug-loading capacity make them ideal nanocarriers for biomedical use. Moreover, their biodegradability attributable to labile coordination bonds allows for safe degradation into non-toxic components under physiological conditions [28]. In cancer therapy, MOFs facilitate site-specific drug delivery and improve therapeutic efficacy through the enhanced permeability and retention (EPR) effect [29]. Their intrinsic porosity also enables efficient diffusion of ROS and the storage or release of gases such as oxygen, making them particularly well-suited for PDT applications [30,31].

UiO-66, a prototypical zirconium-based MOF composed of Zr_6 clusters and 1,4-benzenedicarboxylic acid (BDC) linkers, has attracted considerable attention due to its exceptional thermal and chemical stability [32]. Its structure can be modified post-synthetically to tailor its physicochemical properties for specific therapeutic purposes [33]. Importantly, tumor hypoxia characterized by low oxygen levels and elevated glutathione (GSH) and H_2O_2 concentrations remains a major barrier to PDT, as oxygen is essential for ROS generation [34]. Additionally, PDT itself can worsen hypoxia, contributing to drug resistance and metastasis [35]. Recent advances have demonstrated that nanoscale MOFs can alleviate hypoxia by serving as oxygen carriers or generators, thereby enhancing PDT outcomes [34]. UiO-66's high loading capacity, biocompatibility, tunable porosity, and gas adsorption properties make it a compelling candidate for addressing these limitations. Zirconium-based MOFs, particularly UiO-66, have been increasingly recognized for their advantageous properties in photodynamic therapy applications. Zirconium nodes confer exceptional chemical and thermal stability, while the high porosity and tunable pore size facilitate efficient photosensitizer encapsulation and oxygen storage/release [31,34] Furthermore, the strong Zr–O coordination bonds provide structural robustness under physiological conditions, which is critical for maintaining photophysical performance during PDT [36]. These properties collectively contribute to enhanced singlet oxygen generation, improved photosensitizer stability, and sustained photodynamic activity, making UiO-66 a promising platform for IR783 delivery [37,38]. In this study, a multifunctional nanosystem was developed by encapsulating the near-infrared dye IR783 into UiO-66 MOF (IR783@UiO-66) to enhance breast cancer treatment. This approach aims to address the limitations of IR783, including its poor stability, rapid degradation in polar solvents, low quantum yield, and limited tumor-targeting ability, despite its known pro-apoptotic effects in breast cancer cells via mitochondrial fission. Leveraging the nanoscale size and high loading capacity of UiO-66, the combined platform was designed to improve cellular uptake and PDT efficiency. Following structural characterization and biocompatibility assessments, the cytotoxic and phototoxic effects of IR783, UiO-66, and IR783@UiO-66 were evaluated in vitro on MCF-7 and MDA-MB-231 breast cancer cell lines, as well as MCF-10A normal epithelial cells. Phototoxicity was examined under LED light at varying doses (18–144 J/cm²) and exposure times (7.5–60 min). To further evaluate the impact of UiO-66 encapsulation on photodynamic efficiency, singlet oxygen generation was comparatively assessed before and after IR783 loading using both DPBF and ABDA chemical probes. Results demonstrated that both IR783@UiO-66 and free IR783 significantly reduced cancer cell viability in a dose- and light-dependent manner, while exhibiting minimal cytotoxicity toward normal cells. In contrast, UiO-66 alone showed negligible phototoxicity under identical conditions. The slightly reduced efficacy observed for the loaded system compared to free IR783 is likely attributable to slower dye release kinetics and potential inefficiencies in loading capacity.

2. Materials and methods

2.1. Materials

Zirconyl chloride octahydrate ($ZrOCl_2 \cdot 8H_2O$) and terephthalic acid (BDC) were purchased from Xi'an Ruixi Biotechnology Co., Ltd. IR783 and all other chemicals were obtained from Sigma-Aldrich, unless otherwise specified.

10.57647/pibm-2025-17593

2.2. Synthesis of UiO-66 and IR783@UiO-66 Nanoparticles

UiO-66 nanoparticles were synthesized by making minor modifications to the methods previously reported in the literature. In a typical procedure, zirconyl chloride octahydrate ($ZrOCl_2 \cdot 8H_2O$ 1.6 g, 5.0 mmol) and terephthalic acid (BDC 0.80 g, 4.8 mmol) were dissolved in N,N-dimethylformamide (DMF 30 mL) at room temperature. Then, formic acid (15.0 mL, 397.5 mmol) was added to the mixture and stirred at 140 °C for 2 h using a reflux apparatus. The resulting white precipitate was cooled to room temperature, then filtered and washed once with 20 mL of DMF and 50 mL of acetone and dried to obtain white UiO-66 nanoparticles [39].

To synthesize IR783-loaded UiO-66 nanoparticles (IR783@UiO-66), 100 mg of UiO-66 was dispersed in 25 mL of deionized water under ultrasonic agitation. Subsequently, 5 mL of aqueous IR783 solution (8, 1.4, 2, 1, and 0.5 mg/mL) was added dropwise to the dispersion and stirred in the dark for 3 h to allow dye adsorption. The resulting green-colored IR783@UiO-66 nanoparticles were collected by centrifugation and washed repeatedly with deionized water until the supernatant became colorless, indicating that unbound dye was removed. The final product was dried at room temperature to obtain a dry powder [33]. All steps were carried out under light-protected conditions to prevent photodegradation of the dye.

2.3. Characterization of UiO-66 and IR783@UiO-66 Nanoparticle

2.3.1. *Structural Characterization*

The synthesized UiO-66 and IR783@UiO-66 nanoparticles were characterized using various analytical techniques. Particle size and zeta potential were determined by Dynamic Light Scattering (DLS) (Nano Particle Size Analyzer, Particulate Systems–NanoPlus) to evaluate colloidal stability and predict cellular uptake behavior. Scanning Electron Microscopy (SEM) (FEI QUANTA 250 FEG) and Scanning Transmission Electron Microscopy (STEM) (FEI QUANTA 250 FEG equipped with a STEM detector) were used to assess morphology and particle size, while Energy-Dispersive X-ray Spectroscopy (EDX) (FEI QUANTA 250 FEG) confirmed elemental composition. Crystallinity and phase A dialysis membrane with a molecular weight cut-off (MWCO) of 14,000 Da (34 mm, TX0111, BioBasic) was employed to separate the nanoparticle dispersion from the release medium. Aliquots were withdrawn at predetermined time intervals, and the concentration of purity were analyzed by X-ray Diffraction (XRD) (Philips X'Pert Pro Diffractometer - Royal Philips Electronics, Amsterdam, The Netherlands), and functional groups were identified using Fourier Transform Infrared Spectroscopy (FT-IR) (PerkinElmer Spectrum Two FTIR Spectrometer). Thermogravimetric Analysis (TGA) (Perkin Elmer Diomand TG/DTA) evaluated thermal stability, and Brunauer–Emmett–Teller (BET) analysis was used to determine surface area and porosity.

2.4. IR783 Loading Efficiency

The loading efficiency of IR783 into UiO-66 nanoparticles was determined using UV–Visible spectrophotometry (Shimadzu-UV-2550, Japan and PekinElmer LAMBDA Bio+). A standard calibration curve was first generated by measuring the absorbance of IR783 solutions at 783 nm, its maximum absorption wavelength, using known concentrations. Following the synthesis of IR783@UiO-66, the nanoparticle suspension was centrifuged at 13,500 rpm for 15 minutes to separate unbound IR783. The absorbance of the supernatant was measured, and the concentration of unencapsulated dye was calculated based on the standard curve. The loading and encapsulation efficiency were then determined using the following equations:

$$\text{Drug Loading Efficiency } \% = \frac{\text{Amount of IR783 encapsulated}}{\text{Total amount of nanoparticle}} \times 100$$

$$\text{Encapsulation Efficiency } \% = \frac{\text{Amont of IR783 encsapsulated}}{\text{Amount of the prepared solution of IR783}} \times 100$$

2.5. IR783 Release Profile from UiO-66 Nanoparticles

The release profile of IR783 from IR783@UiO-66 nanoparticles was evaluated using a dialysis method. In this technique, a dialysis membrane serves to retain the nanoparticles while allowing the free drug to diffuse into the surrounding release medium.

For the experiment, IR783@UiO-66 nanoparticles were dispersed in phosphate-buffered saline (PBS) at pH 7.4 and 5.5, and incubated at 37 °C with gentle agitation.

released IR783 was quantified by measuring the absorbance at 783 nm using a UV-Vis spectrophotometer. The cumulative release of IR783 was calculated and plotted as a function of time. The release kinetics were assessed under both neutral and acidic pH conditions to

10.57647/pibm-2025-17593

simulate physiological and tumor microenvironments, respectively. This analysis provided insights into the stability and controlled release capability of the UiO-66 nanocarrier. The cumulative release percentage of IR783 was determined using the following equation[40]:

$$\text{Cumulative release percentage } \% = \frac{Mr}{Mt} \times 100$$

where M_r is the mass of IR783 release from IR783@UiO-66 nanoparticles , M_t is the total mass of loaded IR783.

2.6. Biocompatibility Assessment

The biocompatibility of IR783 and synthesized UiO-66, IR783@UiO-66 nanoparticles was evaluated by serum protein binding capacity and hemolysis assays. The serum protein binding capacity of UiO-66 and IR783@UiO-66 nanoparticles was evaluated using a modified version of the method described by Cole et al. and Semete et al. [41,42]. Various volume ratios of fetal bovine serum (FBS) to IR783@UiO-66 nanoparticle suspensions were prepared (20:80, 40:60, 50:50, 60:40, and 80:20) to a final volume of 500 µL (v/v). The mixtures were incubated at 37 °C with gentle shaking at 150 rpm for 2 hours to allow protein–nanoparticle interactions. Following incubation, the samples were centrifuged at 14,000 rpm for 10 minutes to separate protein-bound nanoparticles from unbound proteins. The resulting pellets were washed twice with phosphate-buffered saline (PBS, pH 7.5), and the supernatants were collected after each wash. The initial FBS sample and all three collected supernatants were analyzed for protein concentration using the Bradford assay [43]. The amount and percentage of serum proteins bound to the IR783@UiO-66 nanoparticles were calculated based on the difference between the initial and residual protein concentrations in the supernatants using the following formula:

$$\text{Protein Binding } \% = \frac{\text{Concn (Initial protein)} - \text{Concn (unbound protein)}}{\text{Concn (initial protein)}} \times 100$$

The hemocompatibility of IR783, UiO-66, and IR783@UiO-66 nanoparticles was assessed by evaluating their hemolytic potential. The extent of hemolysis was determined according to the protocols described by Mayer et al. [44] and Yallapu et al. [45]. Whole blood collected into EDTA tubes was centrifuged at 13,500 rpm for 15 min to isolate erythrocytes. The resulting red blood cells were washed twice with phosphate-buffered saline (PBS) and resuspended in PBS. The erythrocyte suspension was then incubated with IR783, UiO-66 and IR783@UiO-66 nanoparticles at concentrations of 1, 20, and 50 µg/mL at a 1:1 volume ratio (v/v) at 37 °C for 6 h. PBS and 1% Triton X-100 were used as negative and positive controls, respectively. After incubation, all samples were centrifuged at 4,100 rpm for 10 min to remove nanoparticles. Supernatants were collected, and hemoglobin release was measured spectrophotometrically at 540 nm. The percentage of hemolysis was calculated using the following formula:

$$\text{Hemolysis } \% = \frac{\text{Absorbance (sample)} - \text{Absorbance (negative control)}}{\text{Absorbance (positive control)}} \times 100$$

2.7. Evaluation of the photodynamic properties of the synthesized nanoparticles

2.7.1. *Singlet oxygen generation (SOG) assay*

The ability of IR783@UiO-66 nanoparticles to generate singlet oxygen ($^1O_2$) was assessed using two established chemical probes: 1,3-diphenylisobenzofuran (DPBF) and 9,10-anthracenediyl-bis(methylene)dimalonic acid (ABDA). For the DPBF assay, IR783@UiO-66 nanoparticles were prepared at concentrations of 5, 10, 20, 50, 100, and 200 µg/mL and incubated with an 8 mM solution of DPBF in a suitable solvent. DPBF reacts with singlet oxygen to form 1,2-dibenzoylbenzene, resulting in a measurable decrease in its characteristic absorbance peak at 410 nm. Samples were irradiated using a 630 nm LED light source (output power: 40 mW, energy dose: 144 J/cm², exposure time: 3600 s). Absorbance spectra were recorded using a microplate reader before and after irradiation. The percentage reduction in absorbance at 410 nm was used to quantify singlet oxygen generation, as previously described [46]. To further confirm $^1O_2$ production under physiologically relevant conditions, ABDA was employed as a complementary water-soluble probe. IR783 and IR783@UiO-66 (at 5, 10, 20, 50, 100, and 200 µg/mL) were incubated with ABDA (20 µM) in phosphate-buffered saline (PBS). The samples were exposed to 630 nm LED irradiation under identical conditions (40 mW, 144 J/cm², 3600 s), and the absorbance at 378 nm was measured before and after light exposure. The decrease in ABDA absorbance was directly correlated with singlet oxygen production [47].

2.8. Photostability

The photostability of free photosensitizer IR783 and IR783@UiO-66 nanoparticles was evaluated under 630 nm LED irradiation according to a modified method

described by Usama et. al. [48]. Samples were prepared at 10 µM concentration in dimethyl sulfoxide (DMSO).
The decrease in absorbance at 630 nm was monitored using a fluorescence spectrophotometer. Measurements were recorded every 2 min for the first 10 min and then every 10 min for a total of 60 min. The photostability profile was evaluated by plotting the decrease in absorbance as a function of irradiation time .

2.9. Fluorescence quantum yield measurements

The fluorescence emission spectra of the free photosensitizer IR783 and IR783@UiO-66 nanoparticles were recorded using an Edingburg FS-5 spectrophotometer.
The measurements were carried out DMSO where the samples were placed in 1 cm path length quartz cuvettes and excited. The emission was integrated over the 550–800 nm range and all samples were prepared such that their maximum absorbance was below 0.1 to minimize internal filter effects. A solution of free IR783 in DMSO was used as an internal standard for quantum yield calculations. The fluorescence quantum yields of IR783 and IR783@UiO-66 nanoparticles were calculated by the instrument [49].

2.10. Fluorescence lifetime detection

The fluorescence lifetime emission spectra of free photosensitizer IR783 and IR783@UiO-66 nanoparticles were recorded using an Edingburg FS-5 spectrophotometer. Each sample was placed in 1 cm path length quartz cuvettes and excited in DMSO. The fluorescence lifetimes of IR783 and IR783@UiO-66 nanoparticles were measured by the instrument and the fluorescence lifetimes were calculated using the results [50,51].

2.11. In vitro evaluation of synthesized nanoparticles

2.12. Cell lines and culture conditions

In this study, two human breast adenocarcinoma cell lines (MDA-MB-231 and MCF-7) and one non-tumor forming epithelial cell line (MCF-10A) were used to evaluate the The light intensities were calculated according to the formula below.

$$\text{Energy density (J/cm2)} = \frac{\text{Power (W)}}{\text{Area (cm2)}} \times 100$$

After irradiation, 5 µg/mL MTT was added and incubated at 37°C for 3.5 h. The obtained formazan crystals were dissolved in DMSO and the absorbance was measured at

biological effects of the synthesized nanoparticles. MCF-7 and MDA-MB-231 cells were cultured in DMEM medium, while MCF-10A cells were maintained in DMEM/F-12 medium. 10% fetal calf serum (FBS), 1% L-glutamine, and 1% penicillin/streptomycin were added to DMEM medium, while 5% horse serum, 1% pen/strep, 10 µg/mL insulin, 20 ng/mL hEGF, 0.5 ng/mL hydrocortisone, and 100 ng/mL chlorotoxin were added to DMEM/F-12 medium. Cultures were incubated at 37°C in a humidified 5% CO_2 atmosphere. Subculturing was performed when cells reached 80% confluence, and only actively dividing cells in the logarithmic growth phase were used in the experiments.

2.13. Cell viability and cytotoxicity assay

To assess cytotoxicity, MDA-MB-231, MCF-7, and MCF-10A cells were seeded in 96-well plates at a density of 5×103 cells/mL (100 µL per well) and incubated for 24 h. After incubation, the medium was treated with various concentrations (2.5–200 µg/mL) of IR783 and UiO-66, IR783@UiO-66 nanoparticles.
The nanoparticles were sterilized by UV irradiation before cell treatment. Cell viability was determined using the MTT assay after 12, 24, and 48 h of incubation. 10 µL of MTT solution (5 mg/mL PBS) was added and incubated at 37 °C for 3.5 h.
The plates were then centrifuged at 1800 rpm for 10 min and the supernatant was removed. The obtained formazan crystals were dissolved in DMSO and the absorbance was measured at 570 nm using a microplate reader (Thermo Fisher Scientific Multiskan GO). Cell viability was calculated as previously described [52].

2.14. Phototoxicity assay

For phototoxicity analysis, MDA-MB-231, MCF-7, and MCF-10A cells were seeded in 96-well plates at 5×10^3 cells/mL per well and incubated for 24 h. After incubation, the cells were treated with various concentrations of IR783 and UiO-66, IR783@UiO-66 nanoparticles (5–50 µg/mL).
After 24 h of incubation LED light (light intensities of 18, 36, 72, and 144 J/cm²) with 40 mW output power was applied for different times (7.5, 15, 30, and 60 min).
570 nm using a microplate reader (Thermo Fisher Scientific Multiskan GO). Cell viability was calculated as previously described [52].

2.15. Reactive species (ROS) level detection

Cells at a concentration of 5×10^3 cells/mL were incubated in an incubator with 95% humidity and 5% CO_2 using

MDA-MB-231, MCF-7, and MCF-10A 96-well well plates for 24 h and treated with IR783, UiO-66, and IR783@UiO-66 for 24 h. After incubation, the well plates were irradiated with LED light (0.04 W) for 60 min. In order to compare the effects of two different environments on the amount of ROS, the same procedures were carried out in the dark. Then, all samples were washed with PBS (2×) and then reacted with 2',7'-dichlorofluorescin diacetate (DCFH-DA, 10 µM) for 30 min at 37 ˚C in cell culture medium. Relative fluorescence intensity was measured with a UV-vis spectrophotometer (Excitation Wavelength (Ex) = 560 nm and Emission Wavelength (Em) = 612 nm).

2.16. Apoptosis analysis

The apoptotic effects of the samples used in this study on MCF-7, MDA-MB-231, and MCF-10A cell lines were evaluated using the Annexin V-FITC kit. For this purpose, 1980 µL of cell suspension at a concentration of 3×10^5 cells/mL was seeded into 6-well cell culture plates. The cells were incubated at 37 °C in a humidified atmosphere containing 5% CO_2 for 24 hours. Subsequently, the samples were added at a final concentration of 50 µg/mL (prepared in DMSO) to bring the total volume to 2 mL per well. To evaluate the PDT effect, LED light at an output power of 40 mW was applied to the treated cells for 60 minutes, corresponding to a light dose of 144 J/cm². The cells were then incubated for an additional 24 hours. Parallel experiments were conducted in the dark to assess the specific contribution of light activation and to compare apoptotic responses under light and dark conditions. Following incubation, all cells were washed with cold PBS, harvested using trypsin, and centrifuged at 800 rpm for 5 minutes. The resulting pellet was resuspended in 5 mL of cold PBS and centrifuged again. The final pellet was then resuspended in 50 µL of binding buffer, followed by the addition of 2.5 µL of Annexin V-FITC and 5 µL of propidium iodide (PI). The cells were incubated at room temperature in the dark for 15 minutes. After staining, 200 µL of binding buffer was added, and apoptotic analysis was performed using a flow cytometer.

2.17. Statistical analysis

All experiments were performed in triplicate to ensure accuracy and reproducibility. Values are expressed as percentage (%) or mean ± standard deviation of replicates (n=2 or 3). Statistical analysis was done with Excel and GraphPad Prism 9.0.0. MTT analysis results were evaluated by two-tailed paired t-test (for two-group comparison) and one-way ANOVA followed by Tukey multiple comparison test for multiple comparisons (more than two groups). A p-value of <0.05 was considered statistically significant.

2. Results and discussion

3.1. Synthesis and Characterization of UiO-66 and IR783@UiO-66 Nanoparticles

UiO-66 and IR783@UiO-66 nanoparticles were synthesized via a modified solvothermal method, adapting protocols commonly used for metal–organic frameworks to ensure optimal dye encapsulation. Several formulations were prepared by varying the concentration of the near-infrared dye IR783, aiming to optimize encapsulation efficiency, drug loading capacity, and nanoparticle morphology.

Structural analysis was conducted using SEM, DLS, and EDX. Among the tested formulations, the nanoparticles synthesized with 2 mg/mL of IR783 exhibited the most favorable physicochemical characteristics, including well-defined morphology in SEM images, high encapsulation efficiency (84.62%), and an optimal drug loading capacity of 9.08%, equivalent to approximately 1.69 mg of IR783 per nanoparticle batch (Table 1). This optimized formulation was subsequently selected for further evaluations.

SEM imaging revealed uniform particle dispersion for both unloaded UiO-66 and IR783@UiO-66 nanoparticles, with mean diameters of 292.0 ± 20 nm and 317.8 ± 43 nm, respectively, as determined by the analysis of 100 individual particles using ImageJ software (Figure 1A, B). These results align with previous studies that describe the crystalline morphology of UiO-66 nanoparticles[53]. DLS analysis reported hydrodynamic diameters of 453.1 ± 13 nm for UiO-66 and 533.8 ± 13.1 nm for IR783@UiO-66, reflecting the expected increase in particle size upon dye encapsulation.

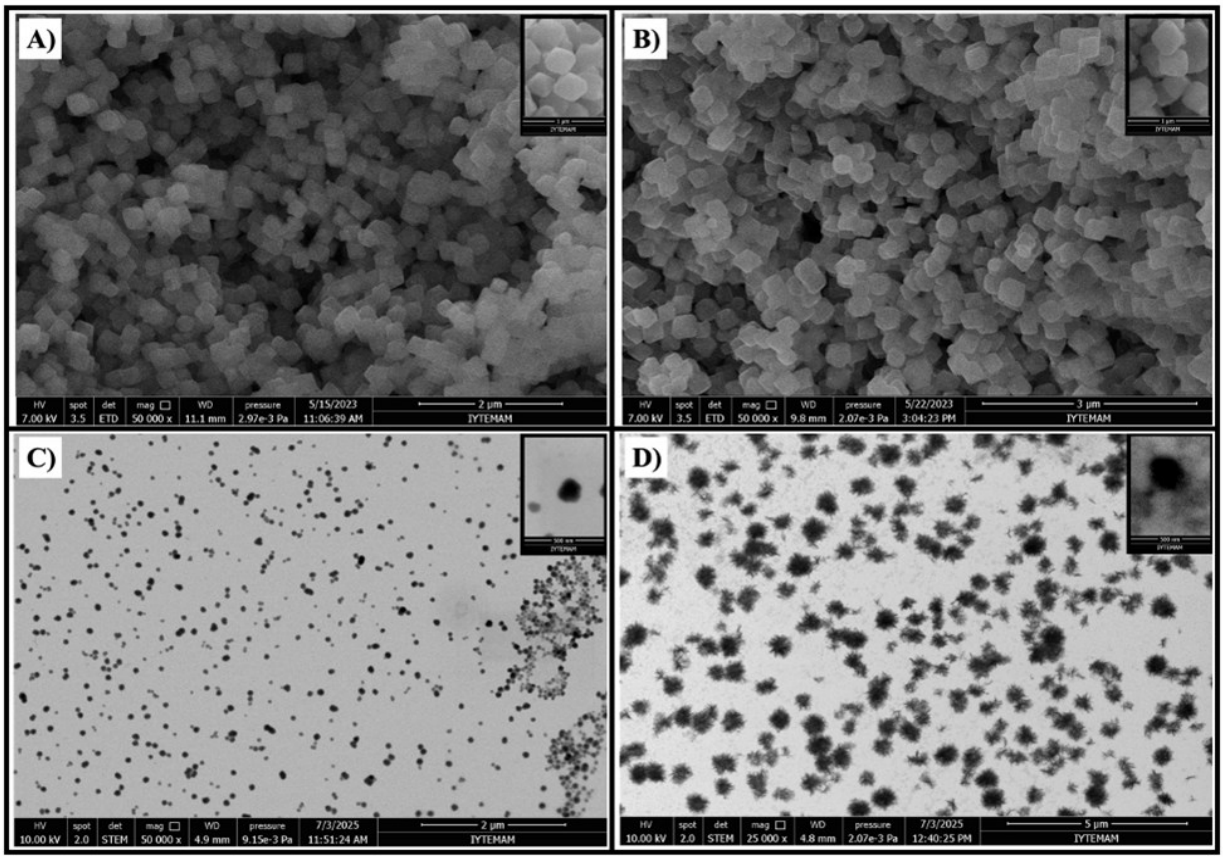

Figure 1. (A) SEM image of UiO-66 nanoparticles; (B) SEM image of IR783@UiO-66 nanoparticles; (C) STEM image of UiO-66 nanoparticles; (D) STEM image of IR783@UiO-66 nanoparticles

Table 1. Physicochemical properties of UiO-66 and IR783@UiO-66 nanoparticles, including particle diameter, hydrodynamic radius, drug loading efficiency, encapsulation efficiency, and zeta potential

Sample	Diameter (nm)	Hydrodynamic radius (nm)	Drug Loading Efficiency (%)	Encapsulation Efficiency (%)	Zeta Potential (mV)
UiO-66	292.0 nm	453.1 nm	-	-	18.91
IR783@UiO-66	317.8 nm	533.8 nm	9.08	84.62	26.30

The discrepancy between SEM and DLS results is attributed to solvation effects and nanoparticle aggregation in suspension, consistent with earlier observations in MOF-based systems [54]. STEM analysis provided further insights into the morphology and dispersion state of the nanoparticles. Figure 1C shows well-dispersed UiO-66 particles with uniform contrast and spherical-to-polyhedral shapes, confirming the monodispersity observed in SEM. In Figure 1D, IR783@UiO-66 nanoparticles appear slightly darker and exhibit increased electron density, indicative of successful dye loading. The absence of significant agglomeration in both images supports good colloidal stability, while the clear particle boundaries reinforce the nanoscale integrity of the structures post-encapsulation. Polydispersity index measurements indicated a narrow size distribution for both nanoparticle formulations, comparable to values reported in other MOF-related studies [28]. Additionally, zeta potential analysis revealed positive surface charges of +18.91 ± 1.76 mV for UiO-66 and +26.30 ± 1.61 mV for IR783@UiO-66, suggesting stable colloidal behavior and the potential for enhanced cellular interactions. This increase in surface charge following IR783 loading is likely due to the ionic functional groups present in the dye, facilitating favorable electrostatic interactions with negatively charged cell membranes [28]. EDX elemental analysis confirmed successful dye encapsulation.

While the elemental composition of UiO-66 matched its theoretical formula ($C_{48}H_{28}O_{30}Zr_6$), the detection of sodium (Na), sulfur (S), and chlorine (Cl) peaks in the IR783@UiO-66 spectrum was consistent with the molecular structure of IR783 ($C_{38}H_{46}ClN_2NaO_6S_2$), supporting effective dye integration within the MOF framework [55]. FTIR spectroscopy was used to verify the structural integrity of UiO-66 and confirm IR783 encapsulation within the

10.57647/pibm-2025-17593

nanoparticle matrix (Figure 2A). The FTIR spectrum of IR783 showed characteristic bands for C–H stretching (3000–3100 cm^{-1}), C=C and C=N stretching (1500–1650 cm^{-1}), and S=O stretching (1030–1080 cm^{-1}), consistent with previous reports on cyanine dyes [56]. UiO-66 exhibited typical signals from the terephthalic acid linker, including carboxylate stretching at 1597 and 1406 cm^{-1}, and the absence of a peak at 1685 cm^{-1} confirmed complete linker coordination [57]. The IR783@UiO-66 spectrum displayed vibrational features of both the dye and MOF framework, suggesting successful dye integration. Although FTIR cannot conclusively distinguish between surface adsorption and internal encapsulation, the coexistence of these signals, along with the absence of IR783 peaks in unloaded UiO-66, supports effective dye incorporation into the MOF structure. Complementary visual evidence for successful encapsulation was provided by the observable color change of the nanoparticles. While UiO-66 nanoparticles appeared white, IR783-loaded samples exhibited a distinct green coloration, consistent with dye incorporation. Such colorimetric shifts have been widely reported as indicative of successful dye loading into porous nanocarriers [57]. XRD analysis was performed to evaluate the crystallinity of UiO-66 nanoparticles and to confirm framework integrity after IR783 encapsulation (Figure 2B). UiO-66 exhibited characteristic diffraction peaks at 2θ values of 7.37°, 8.57°, and 25.72°, consistent with the (111), (002), and (022) planes, matching previous reports [33]. These peaks were retained in the IR783@UiO-66 pattern, indicating preserved crystalline structure after dye loading. However, a reduction in peak intensity suggested partial loss of long-range order, likely due to guest molecule incorporation within the pores [58]. Additionally, the diminished diffraction signals of crystalline IR783 in the loaded formulation implied that the dye was predominantly encapsulated in an amorphous or molecularly dispersed state, favorable for enhancing solubility and bioavailability.

Overall, the results confirm successful dye incorporation without compromising MOF structural integrity.

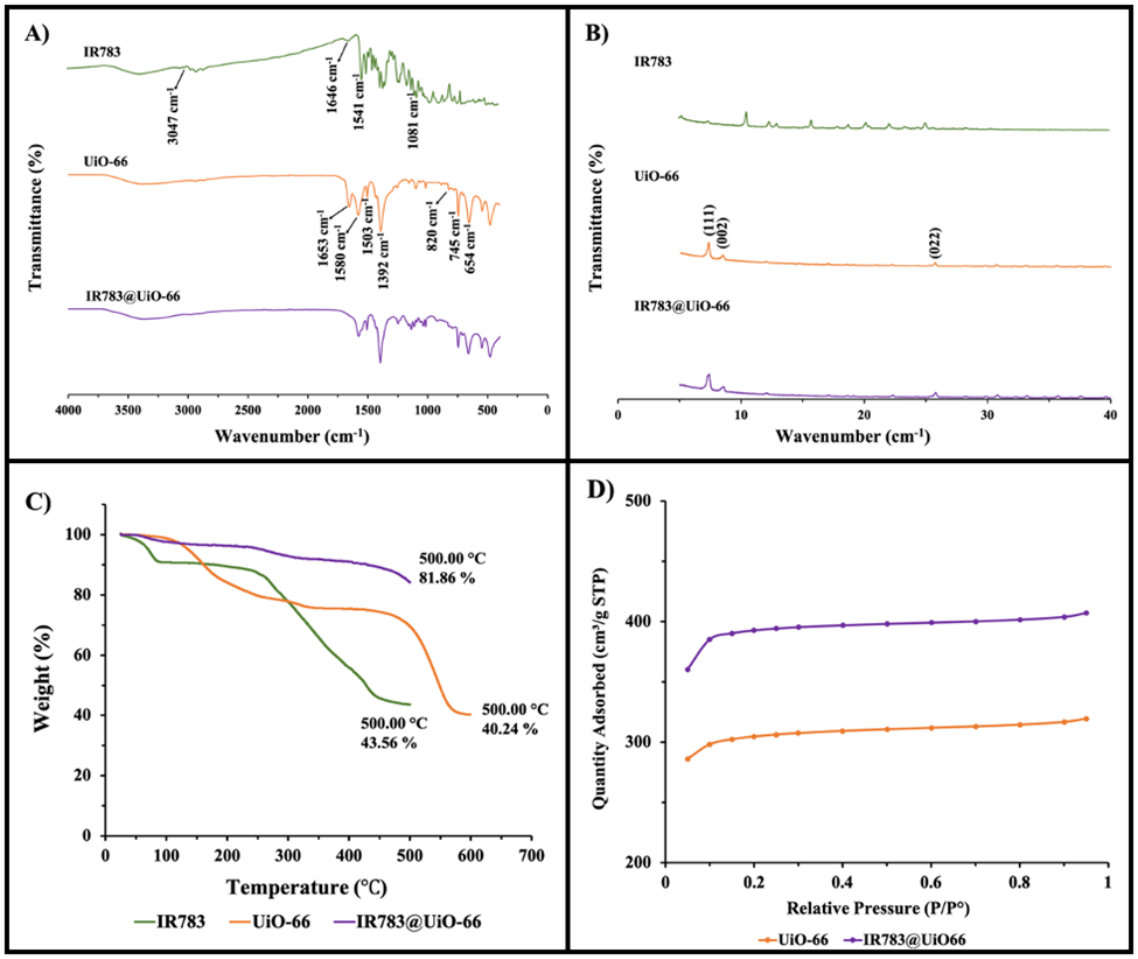

Figure 2. (A) FTIR spectra of IR783, UiO-66, and IR783@UiO-66; (B) XRD patterns of IR783, UiO-66, and IR783@UiO-66; (C) TGA curves of IR783, UiO-66, and IR783@UiO-66; (D) Nitrogen adsorption–desorption isotherms of UiO-66 and IR783@UiO-66

10.57647/pibm-2025-17593

TGA was performed to assess the thermal stability and decomposition behavior of IR783, UiO-66, and IR783@UiO-66 nanoparticles (Figure 2C). Free IR783 exhibited a multi-stage decomposition, with the most significant weight loss (43.56%) between 55 °C and 500 °C, consistent with the thermal degradation of its organic components [59]. In comparison, unloaded UiO-66 showed three distinct weight loss stages, corresponding to water desorption (~90 °C), removal of residual DMF, and framework decomposition with ZrO_2 formation around 599 °C, in line with previous reports [60]. The IR783@UiO-66 nanocomposite displayed a similar profile, confirming structural integrity after dye loading. Notably, the higher initial weight loss (81.86% between 30 °C and 500 °C) reflected the combined degradation of both the MOF structure and encapsulated IR783, supporting high dye loading and successful incorporation within the framework. MOFs are known for their high porosity and large surface areas. To evaluate the textural properties of UiO-66 and IR783@UiO-66 nanoparticles, nitrogen adsorption–desorption measurements were performed, and the BET surface area, pore size distribution, and pore volume were determined (Figure 2D). Both samples exhibited Type I isotherms, characteristic of microporous materials, indicating that dye loading did not compromise the structural integrity of the UiO-66 framework.

The BET and Langmuir surface areas were calculated as 922.76 m^2/g and 1188.80 m^2/g for UiO-66, respectively. A slight decrease in surface area was observed for IR783@UiO-66, attributed to interactions between the Zr_6 clusters and the sulfonic acid groups of IR783, rather than simple pore blockage by dye encapsulation, consistent with previous findings [33]. The minimal change in pore size further supports that the microporous structure of UiO-66 remained largely unaffected after dye incorporation. These results align well with reported data for dye-loaded MOF systems.

3.2. pH-Dependent release profile of IR783 from UiO-66 nanoparticles

The pH-responsive release behavior of IR783@UiO-66 was investigated under conditions simulating the tumor microenvironment (pH 5.0) and normal physiological conditions (pH 7.4). Such pH-dependent release profiles are critical for enhancing the therapeutic index of nanocarrier systems by promoting targeted drug accumulation at acidic tumor sites while minimizing systemic toxicity [61,62].

The IR783@UiO-66 nanoparticles were dispersed in phosphate-buffered saline (PBS, pH 7.4) and acetate buffer (pH 5.0) and incubated at 150 rpm for four days.

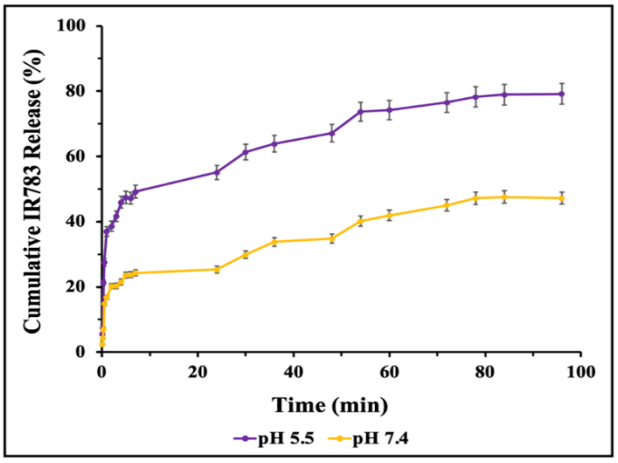

Figure 3. pH-dependent release study of IR783 from IR783@UiO-66 nanoparticles. Release profiles were monitored at pH 7.4 (physiological) and pH 5.0 (tumor-simulated) over 96 hours using UV–Vis spectroscopy. Data are presented as mean ± SD (n = 3)

At defined time intervals, supernatant samples were collected, and the released IR783 content was quantified via UV–Vis spectrophotometry, using the characteristic absorbance peak of the dye. As shown in Figure 3, the release of IR783 was significantly accelerated at pH 5.0 compared to pH 7.4. After 96 hours, the cumulative release of IR783 reached approximately 71% at acidic pH, whereas only 34% was released under neutral conditions. This enhanced release at lower pH is likely attributed to the partial destabilization of metal–ligand coordination bonds in the UiO-66 framework under acidic conditions, which facilitates the diffusion of encapsulated dye molecules. The observed pH-sensitive release behavior is consistent with previous reports on MOF-based nanocarriers, where acidic environments trigger selective drug release by weakening the interaction between the MOF framework and the guest molecules [61]. These results confirm that IR783@UiO-66 exhibits effective pH-responsive release properties, supporting its potential application as a smart drug delivery system for tumor-targeted PDT.

3.3. Biocompatibility evaluation of IR783@UiO-66 nanoparticles

3.3.1. *Protein binding assay*

The interaction of nanoparticles with plasma proteins significantly affects their biodistribution, cellular uptake, and clearance rates. Protein adsorption studies were performed to evaluate the binding of serum proteins to IR783@UiO-66 nanoparticles, using fetal bovine serum (FBS) as a model system. Nanoparticles were incubated with varying serum-to-nanoparticle ratios (20:80 to 80:20) at 37 °C for 2 hours to simulate physiological conditions.

10.57647/pibm-2025-17593

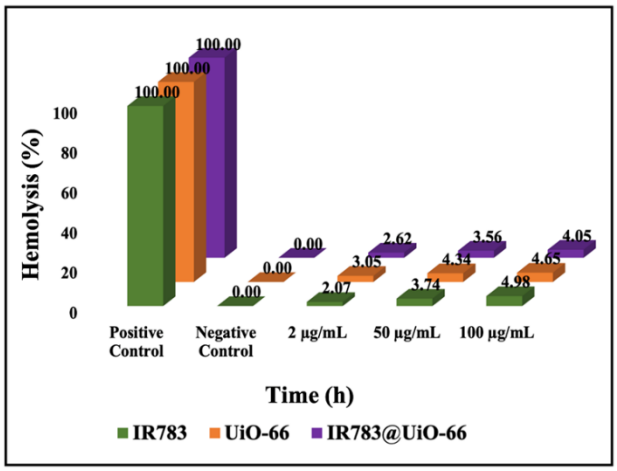

Figure 4. Hemolysis assay of IR783, UiO-66, and IR783@UiO-66 nanoparticles. Blood compatibility was evaluated at concentrations of 1, 20, and 50 µg/mL using a standard hemolysis assay

Table 2. Binding percentages of IR783 dye, UiO-66, and IR783@UiO-66 nanoparticles to serum proteins

	Protein Binding (%)		
V_{serum}:$V_{nanoparticle}$	IR783	UiO-66	IR783@UiO-66
20:80	5.48	0.3	6.82
40:60	8.40	0.14	7.68
50:50	14.10	3.56	3.65
60:40	6.37	9.71	3.37
80:20	16.81	7.11	6.32

The concentration of unbound serum proteins in the supernatant was measured using the Bradford assay [43]. Results demonstrated low serum protein binding across all tested nanoparticle formulations (Table 2), indicating favorable biocompatibility and suggesting minimal opsonization, a desirable feature for prolonged circulation and reduced immune recognition. These findings are consistent with previous studies highlighting the role of positive surface charge and particle size in modulating protein corona formation [63].

3.4. Hemolysis assay

The hemolytic potential of the nanoparticles was assessed to determine their compatibility with erythrocytes (red blood cells). Nanoparticles were incubated with human erythrocytes at concentrations of 2, 50, and 100 µg/mL, and hemoglobin release was quantified spectrophotometrically. Triton X-100 and PBS served as positive and negative controls, respectively. As shown in Figure 4, all nanoparticle formulations exhibited hemolysis levels below 5%, well within the acceptable range for blood-compatible materials. Notably, IR783@UiO-66 nanoparticles displayed comparable or lower hemolytic activity than free IR783, suggesting that encapsulation within the MOF matrix mitigates potential cytotoxic effects on red blood cells. These results align with previous reports indicating that nanoparticle surface charge and size influence hemolytic activity [44,64]. Together, these biocompatibility assays confirm the safety of IR783@UiO-66 nanoparticles for potential intravenous administration.

3.5. Singlet oxygen generation and photophysical characterization

The photodynamic activity of IR783-loaded UiO-66 nanoparticles (IR783@UiO-66) was evaluated by assessing their singlet oxygen ($^1O_2$) generation capacity using two complementary chemical probes: 1,3-diphenylisobenzofuran (DPBF) and 9,10-anthracenediyl-bis(methylene)dimalonic acid (ABDA). In the DPBF assay, IR783@UiO-66 and bare UiO-66 were tested at concentrations of 5, 10, 20, 50, 100, and 200 µg/mL. Upon 630 nm LED irradiation (40 mW, 144 J/cm², 60 min), a progressive, concentration-dependent decrease in DPBF absorbance at 410 nm was observed in IR783@UiO-66 samples, confirming efficient photoinduced $^1O_2$ production (Figure 5A). The maximum reduction occurred at 200 µg/mL, consistent with previous reports showing enhanced reactive oxygen species (ROS) generation at higher photosensitizer concentrations [28,65]This photobleaching effect, which arises from the reaction between DPBF and singlet oxygen, confirmed the photosensitizing activity of the nanoparticles under light exposure. These results underscore the robust light-activated ROS-generating capacity of the nanoparticle formulation [66]. To further validate $^1O_2$ production under aqueous and physiologically relevant conditions, the ABDA assay was employed. Both free IR783 and IR783@UiO-66 (5–200 µg/mL) were incubated with ABDA (20 µM) in PBS and irradiated under identical conditions (630 nm, 40 mW, 144 J/cm², 3600 s). A measurable reduction in ABDA absorbance at 378 nm was recorded post-irradiation, with IR783@UiO-66 showing significantly greater decreases at all tested concentrations (Figure 5B). This enhancement is attributed to improved photostability, dispersibility, and singlet oxygen quantum yield conferred by MOF encapsulation[28]. Collectively, these findings (summarized in Table 3) confirm that IR783@UiO-66 nanoparticles possess superior singlet oxygen generation efficiency compared to free IR783, supporting their potential as highly effective photosensitizers for PDT. To better understand the mechanism underlying this enhancement, photophysical properties of free IR783 and IR783@UiO-66 were examined.

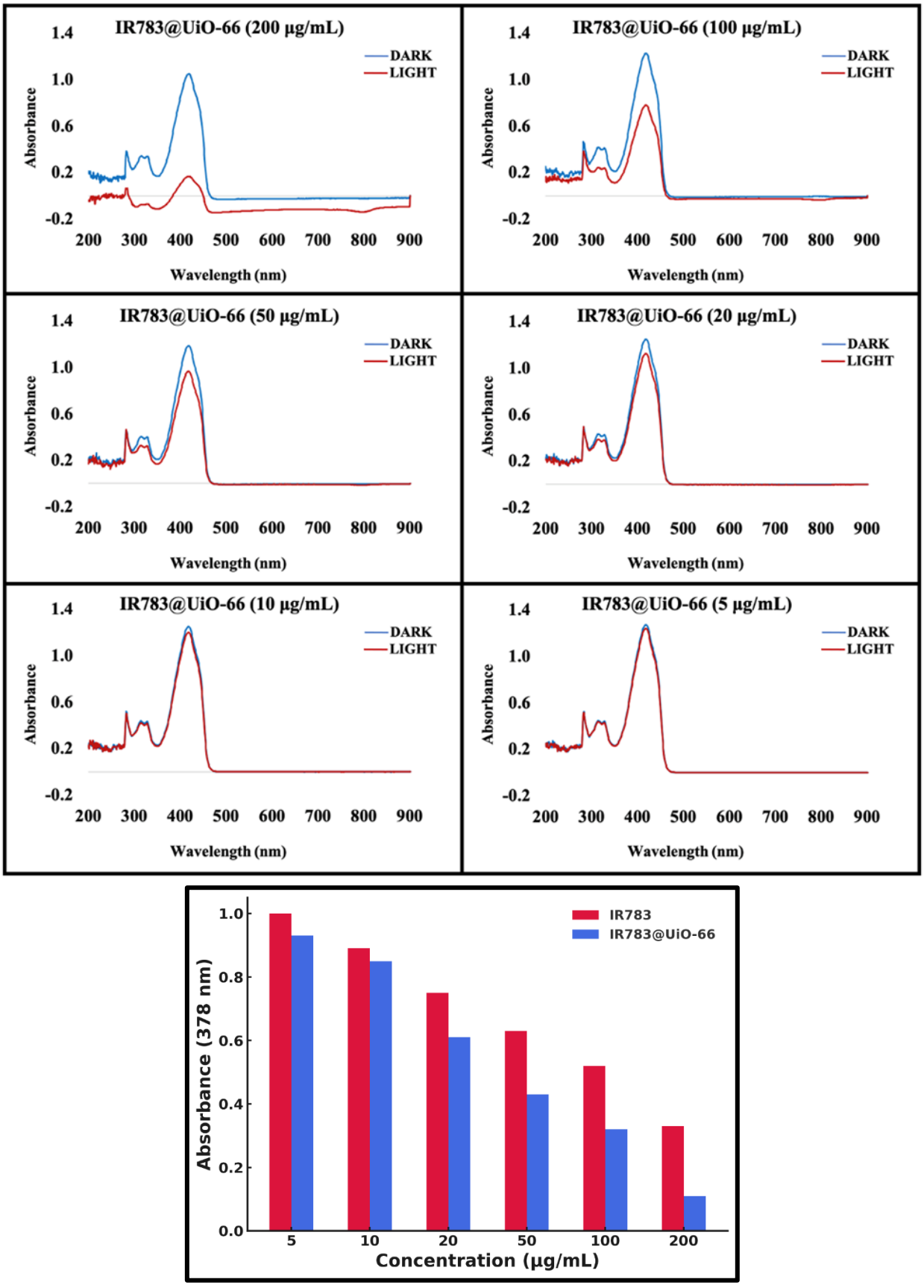

Figure 5. (A) Singlet oxygen generation by IR783@UiO-66 measured using the DPBF assay. DPBF absorbance at 410 nm was monitored under 630 nm LED irradiation (144 J/cm²) to assess concentration-dependent ROS generation for PDT applications. (B) Singlet oxygen generation by IR783 and IR783@UiO-66 assessed using ABDA absorbance at 378 nm following 630 nm LED exposure (40 mW, 144 J/cm², 3600 s) across varying concentrations

10.57647/pibm-2025-17593

Fluorescence quantum yield (ΦF) measurements revealed a marked increase from 0.93% for free IR783 to 3.32% upon UiO-66 encapsulation (Table 4). This increase likely results from reduced aggregation-induced quenching and improved spatial distribution of dye molecules within the MOF pores, which minimizes non-radiative decay[26]. Time-resolved fluorescence studies further support this interpretation. The average fluorescence lifetime (τ_a) of IR783 increased from 11.99 ns in its free form to 33.64 ns when encapsulated. This prolonged lifetime suggests restricted non-radiative relaxation and enhanced intersystem crossing, both of which are beneficial for singlet oxygen production [67].

Table 3. Singlet oxygen generation (%) by IR783@UiO-66 nanoparticles at varying concentrations determined using 1,3-diphenylisobenzofuran (DPBF) and 9,10-Anthracenediyl-bis(methylene)dimalonic acid (ABDA) as a chemical probe

IR783@UiO66 (μg/mL)	SOG (%) with DPBF	SOG (%) with ABDA
200	85.00 %	90.00 %
100	36.68 %	75.21 %
50	18.60 %	60.10 %
20	9.74 %	40.00 %
10	3.88 %	18.48 %
5	2.35 %	5.04 %

Table 4. Fluorescence lifetime and quantum yield values of free IR783 and IR783@UiO-66 nanoparticles

	τ_1 (ns)	τ_2 (ns)	τ_3 (ns)	τ_a (ns)	ϕ_F (%)
IR783	0.532	3.369	44.9699	11.9866	0.928
IR783@ UiO-66	0.9656	4.1533	78.7935	33.6384	3.32

The correlation between improved photophysical properties and $^1O_2$ generation confirms the role of the MOF in stabilizing the dye's excited state and promoting efficient photodynamic action. Although absolute singlet oxygen quantum yields (SOGQY) were not calculated using a standard reference dye, the combination of comparative DPBF/ABDA results and photophysical enhancements provides a robust and reliable assessment of the relative SOGQY before and after IR783 loading. These findings collectively confirm that UiO-66 encapsulation substantially improves the photodynamic performance of IR783, validating the design of the IR783@UiO-66 nanosystem for effective PDT applications.

3.6. Photostability assessment

Photostability is a critical parameter for photosensitizers used in PDT, as excessive photobleaching can diminish therapeutic efficacy by reducing ROS generation during light exposure.

To assess the protective effect of UiO-66 encapsulation, the photostability of free IR783 and IR783@UiO-66 nanoparticles was evaluated under continuous LED irradiation (630 nm, 40 mW) for 60 minutes. Both formulations were prepared at 50 μg/mL in DMSO, and absorbance was recorded at the maximum wavelength of IR783 at regular intervals every 2 minutes for the first 10 minutes, followed by every 10 minutes up to 60 minutes (Figure 6). The results showed that free IR783 experienced a gradual and substantial decrease in absorbance, indicating notable photobleaching over time. In contrast, IR783@UiO-66 maintained significantly higher absorbance levels throughout the irradiation period, demonstrating enhanced photostability. This observed improvement can be attributed to the physical confinement of IR783 molecules within the porous framework of UiO-66, which likely restricts their rotational and vibrational freedom, thereby reducing the likelihood of non-radiative decay and degradation pathways. Additionally, the MOF matrix may provide a shielding effect, protecting the encapsulated dye from direct light-induced damage and limiting its interaction with surrounding reactive species.

These findings are consistent with previous studies reporting enhanced stability of photosensitizers when incorporated into nanocarriers or rigid architectures [68,69]. The superior photostability of IR783@UiO-66 complements the improvements observed in singlet oxygen generation and photophysical properties, further supporting its utility as a robust and efficient nanoplatform for photodynamic therapy.

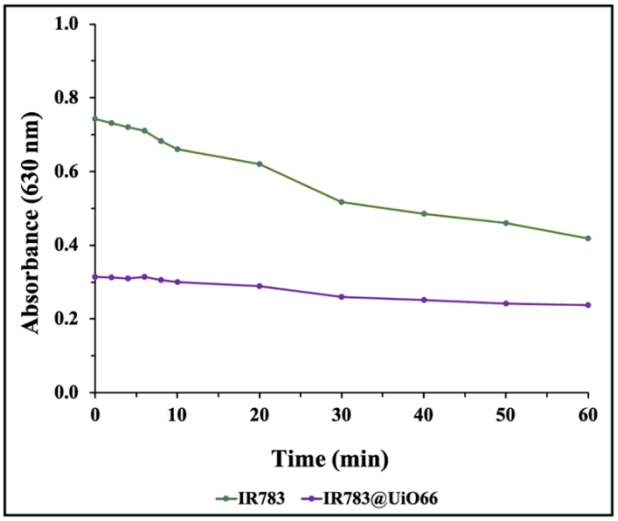

Figure 6. Photostability analysis of free IR783 and IR783@UiO-66. Samples were exposed to 630 nm LED irradiation to compare photobleaching behavior and evaluate the effect of MOF encapsulation on dye stability

3.7. In vitro cytotoxicity, phototoxicity, and ROS generation studies

3.7.1. Cytotoxicity evaluation under dark conditions

The biocompatibility and cytotoxic effects of free IR783, unloaded UiO-66 nanoparticles, and IR783-loaded UiO-66 nanocomposites were systematically evaluated on healthy breast epithelial cells (MCF-10A) and two human breast cancer cell lines (MDA-MB-231 and MCF-7). Cytotoxicity assays were performed using the MTT method at three different incubation periods: 12, 24, and 48 hours. As shown in Figure 7, cell viability decreased in a concentration- and time-dependent manner across all treatment groups. Unloaded UiO-66 nanoparticles exhibited minimal cytotoxicity toward both healthy and cancerous cell lines, even at higher concentrations and extended exposure times (Fig. S1, Fig. S3, Fig. S4). This result supports previous findings regarding the inherent biocompatibility of UiO-66-based nanocarriers [70,71]. In contrast, free IR783 displayed higher cytotoxicity toward healthy MCF-10A cells compared to the cancerous MDA-MB-231 and MCF-7 cells, suggesting non-selective toxicity. Notably, IR783 encapsulation within UiO-66 significantly reduced cytotoxic effects on healthy cells while retaining activity against cancer cells (Fig. S1, Fig. S3, Fig. S4). This protective effect is attributed to controlled dye release and reduced exposure of non-target tissues to free IR783, aligning with earlier studies on MOF-based drug delivery systems [72,73].

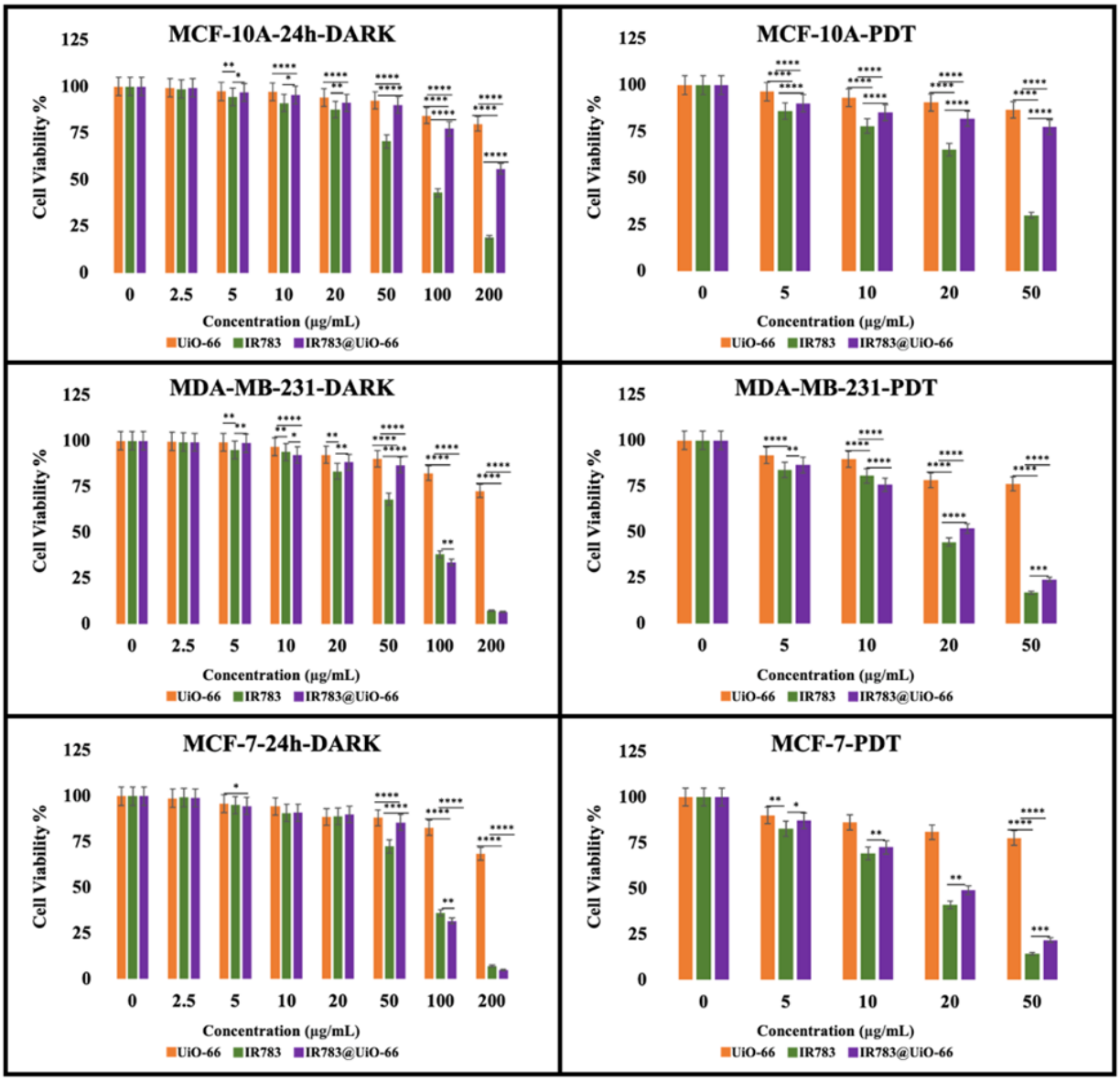

Figure 7. Cytotoxicity and phototoxicity assessment of IR783, UiO-66, and IR783@UiO-66. MCF-10A, MCF-7, and MDA-MB-231 cells were incubated with samples for 24 h, followed by LED irradiation (144 J/cm²) or dark conditions. Cell viability was evaluated using the MTT assay. Statistical analysis was performed using one-way ANOVA (*p < 0.03, **p < 0.02, ***p < 0.002, ****p < 0.0001)

10.57647/pibm-2025-17593

3.8. Phototoxicity evaluation (photodynamic therapy assessment)

Following initial cytotoxicity screening, the photodynamic efficacy of IR783-loaded UiO-66 nanoparticles was systematically evaluated under LED irradiation (630 nm, 40 mW) across varying light doses (18, 36, 72, and 144 J/cm²) and exposure times (7.5, 15, 30, and 60 minutes). Nanoparticle concentrations ranging from 5 to 50 µg/mL were selected based on cytotoxicity results to minimize off-target effects while ensuring therapeutic relevance. Under light exposure, a concentration- and light dose-dependent reduction in cell viability was observed in both cancer cell lines (MCF-7 and MDA-MB-231), with the most pronounced phototoxicity achieved at 144 J/cm² (Fig. 7, Fig. S2, Fig. S4, Fig. S6). Notably, free IR783 exhibited strong phototoxicity but also higher cytotoxicity toward healthy MCF-10A cells. In contrast, IR783@UiO-66 nanoparticles demonstrated enhanced selectivity, effectively reducing cancer cell viability while largely sparing healthy cells, particularly at lower nanoparticle concentrations. The unloaded UiO-66 nanocarrier did not exhibit photodynamic activity, consistent with the absence of intrinsic photosensitizing properties[72]. Among the tested conditions, 50 µg/mL was identified as the most effective concentration for PDT-induced cytotoxicity. While free IR783 exhibited higher immediate cytotoxicity, IR783@UiO-66 achieved comparable photodynamic effects with reduced off-target toxicity, likely due to controlled release dynamics and encapsulation within the MOF framework. These findings highlight the potential of IR783@UiO-66 as an effective and selective photosensitizer system for PDT, offering improved safety profiles by minimizing damage to healthy cells. This selective cytotoxicity underscores the promise of MOF-based delivery systems for enhancing the therapeutic index of PDT agents, providing a strong foundation for future preclinical studies.

3.9. Apoptosis analysis

To confirm that the observed cytotoxicity was due to cell death, apoptosis analysis was conducted using Annexin V-FITC/PI staining followed by flow cytometry. This experiment was performed on MCF-10A (normal), MCF-7, and MDA-MB-231 (cancer) cell lines treated with IR783, UiO-66, and IR783@UiO-66, under both dark and LED-irradiated conditions. As shown in Figure 8, minimal apoptosis was detected in the control and dark-incubated groups, indicating that the compounds themselves do not induce significant toxicity in the absence of light. Upon LED irradiation (144 J/cm²), a marked increase in apoptotic cell populations was observed, particularly in cancer cells treated with IR783@UiO-66. In both MCF-7 and MDA-MB-231 cell lines, IR783@UiO-66 significantly enhanced the percentage of early and late apoptotic cells compared to IR783 or UiO-66 alone, confirming its superior photodynamic effect. Notably, MCF-10A cells exhibited lower apoptotic rates under the same conditions, suggesting selective cytotoxicity toward cancer cells. These findings validate that the reduction in cell viability upon treatment was indeed due to apoptosis, supporting the potential of IR783@UiO-66 as an effective and selective agent for photodynamic cancer therapy.

3.10. ROS generation

Intracellular ROS levels were measured to confirm the mechanism of phototoxicity and assess oxidative stress induction. ROS detection was performed using the fluorescent probe 2′,7′-dichlorodihydrofluorescein diacetate (DCFH-DA), which fluoresces upon oxidation to 2′,7′-dichlorofluorescein (DCF)[74,75]. Cells were treated with IR783, UiO-66, or IR783@UiO-66 for 24 hours, followed by LED irradiation (630 nm, 40 mW) for 60 minutes. The results demonstrated a significant, concentration-dependent increase in ROS generation, with 50 µg/mL producing markedly higher ROS levels than 20 µg/mL across all cell lines. Under light activation, IR783@UiO-66 induced robust ROS production in MDA-MB-231 and MCF-7 cancer cells, while ROS levels remained relatively low in healthy MCF-10A cells (Figure 9). In contrast, free IR783 generated comparable ROS levels in both cancerous and healthy cells, underscoring its limited selectivity. Unloaded UiO-66 nanoparticles did not show significant ROS generation under either condition, confirming the absence of intrinsic photosensitizing activity. Notably, light exposure substantially amplified ROS production for both IR783 and IR783@UiO-66, with the highest levels observed in cancer cells treated with 50 µg/mL IR783@UiO-66 under irradiation. Encapsulation of IR783 within the UiO-66 framework effectively reduced off-target oxidative stress in normal cells while maintaining potent ROS-mediated cytotoxicity in cancer cells, likely due to controlled release and localized dye accumulation. These findings confirm that IR783@UiO-66 nanoparticles enable selective ROS generation upon light activation, offering a promising strategy for enhancing the therapeutic index of PDT. By minimizing collateral damage to healthy tissues and selectively inducing oxidative stress in cancer cells, IR783@UiO-66 represents an effective platform for targeted PDT applications.

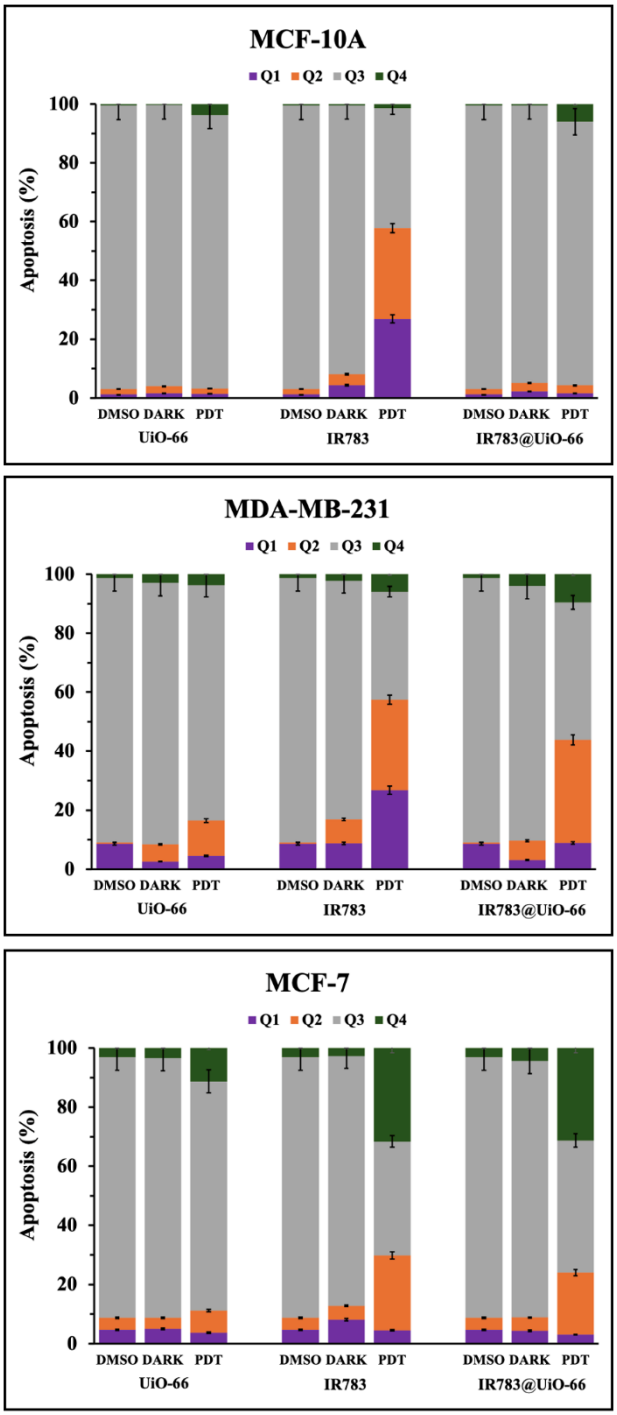

Figure 8. Apoptosis analysis of IR783, UiO-66, and IR783@UiO-66 in MCF-10A, MCF-7, and MDA-MB-231 cell lines following 24-hour incubation under dark conditions and after LED irradiation (144 J/cm²)

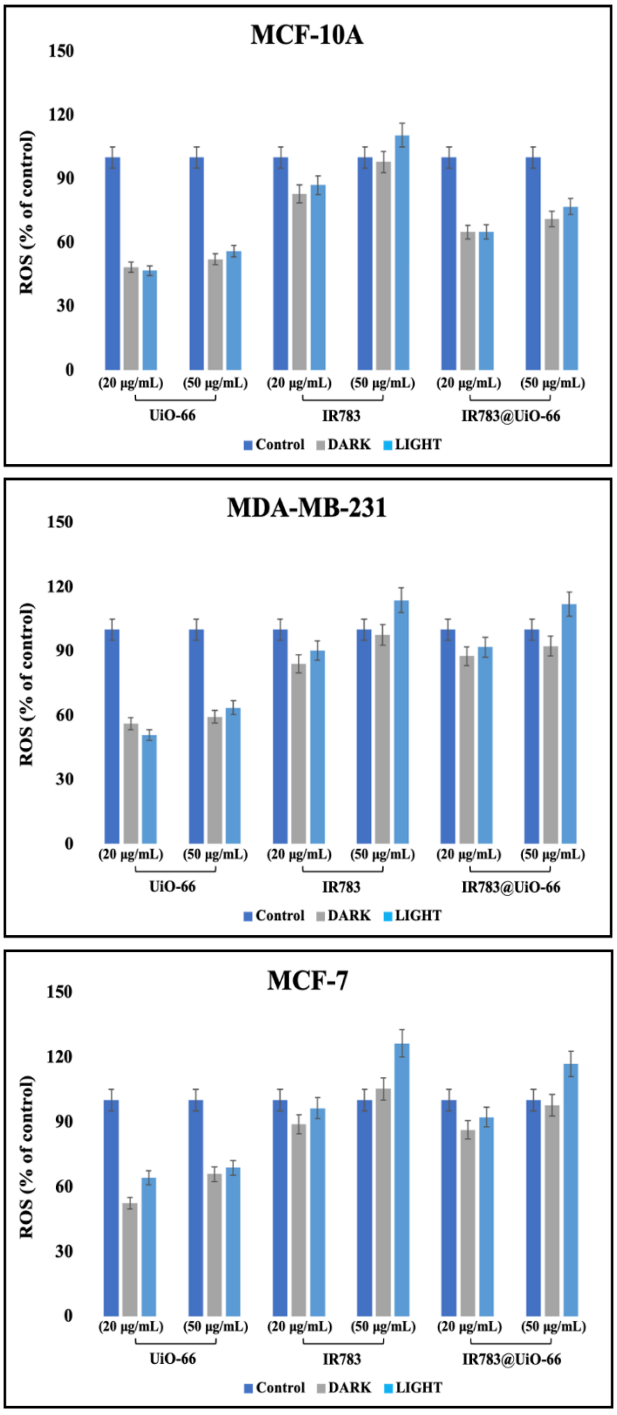

Figure 9. Intracellular ROS levels in MCF-10A, MCF-7, and MDA-MB-231 cells. Cells were treated with IR783, UiO-66, or IR783@UiO-66, followed by incubation with DCFH-DA. ROS levels were measured via fluorescence after 630 nm LED irradiation (60 min) or under dark conditions

3. Conclusion

This study presents a novel nanosystem, IR783@UiO-66, developed to enhance the efficacy of PDT for breast cancer by combining the tumor-targeting properties of IR783 with the high loading capacity and structural stability of the UiO-66 metal–organic framework. Encapsulation of IR783 within the UiO-66 matrix effectively addressed key limitations of the free dye, including poor solubility, low fluorescence quantum yield, and limited tumor selectivity. The resulting nanoplatform exhibited dose- and light-dependent cytotoxicity against breast cancer cell lines (MCF-7 and MDA-MB-231), while maintaining minimal toxicity toward normal epithelial cells (MCF-10A). Although free IR783 demonstrated slightly greater phototoxicity likely

10.57647/pibm-2025-17593

due to faster cellular uptake IR783@UiO-66 offered a more controlled, stable, and biocompatible delivery system. Importantly, a comparative assessment of singlet oxygen generation before and after encapsulation revealed that the MOF architecture significantly enhances photodynamic activity, supported by improved fluorescence lifetime and quantum yield parameters. These findings validate the IR783@UiO-66 nanosystem as a promising photosensitizer delivery platform and highlight the broader potential of UiO-66-based MOFs in PDT applications. Overall, this work underscores the therapeutic promise of IR783@UiO-66 and provides a foundation for further optimization and future in vivo studies targeting breast cancer.

Funding

This research was supported by İYTE AÜDP-2023, under grant number R1-2022IYTE-3-0012. The authors gratefully acknowledge the financial support that made this study possible.

Declaration of competing interest

The authors declare that they have no known competing financial interests or personal relationships that could have appeared to influence the work reported in this paper.

Ethical approval

Not applicable.

Consent to participate

Not applicable.

Consent to publish

Not applicable.

Acknowledgments

The authors would like to thank Biotechnology and Bioengineering Application and Research Center (BIOMER) and The Center for Materials Research (IZTECH-CMR) at İzmir Institute of Technology for the facilities and technical support.

Authors Contribution

S.Ş.: Methodology, Investigation, Data curation, Formal analysis, original draft preparation. G.S.M.: Supervision, Conceptualization, Investigation, Writing - review & editing.

Availability of data and materials

The data that support the findings of this study are available from the corresponding author, upon reasonable request.

Conflict of interests

The authors have no conflicts of interest to declare.

References

[1] Bray F, Ferlay J, Soerjomataram I, Siegel RL, Torre LA, Jemal A. Global cancer statistics 2018: GLOBOCAN estimates of incidence and mortality worldwide for 36 cancers in 185 countries. CA Cancer J Clin. 2018;68(6):394-424. doi: https://doi.org/10.3322/caac.21492

[2] Sampath M, Pichaimani A, Kumpati P, Sengottuvelan B. Breast cancer statistics and emerging trends. Curr Probl Cancer. 2020;44(6):100504.

[3] Leon-Ferre RA, Lau YK, Smith ML, Thompson RA, Hieken TJ, Boughey JC, et al. Male breast cancer: A disease distinct from female breast cancer. Breast Cancer Res Treat. 2018;173(1):37-48.

[4] Ahmad A. Breast cancer statistics: recent trends. Adv Exp Med Biol. 2019;1152:1-7. doi: https://doi.org/10.1007/978-3-030-20301-6_1

[5] Ferlay J, Ervik M, Lam F, Colombet M, Mery L, Piñeros M, et al. Global Cancer Observatory: Cancer Today. Lyon, France: International Agency for Research on Cancer; 2021. Available from: https://gco.iarc.fr/today

[6] Fisher B, Anderson S, Redmond CK, Wolmark N, Wickerham DL, Cronin WM. Reanalysis and results after 12 years of follow-up in a randomized clinical trial comparing total mastectomy, lumpectomy, and lumpectomy plus irradiation. N Engl J Med. 1995;333(22):1456-61. doi: https://doi.org/10.1056/NEJM199511303332203

[7] Houghton J, George WD, Cuzick J, Duggan C, Fentiman IS, Spittle M. Radiotherapy and tamoxifen after breast-conserving surgery. N Engl J Med. 2003;347(16):1233-41. doi: https://doi.org/10.1016/S0140-6736(03)13859-7

[8] Li C, Zhang Y, Wang W, Liu Z, Wang L, Gao W, et al. Advances in nanomedicine for breast cancer treatment. Biomaterials. 2019;221:119416.

[9] Bown SG. Photodynamic therapy for photochemists. Photochem Photobiol Sci. 2013;12(7):1187-90.

[10] Cengel KA, Simone CB, Glatstein E. PDT: mechanisms and clinical use. J Clin Oncol. 2016;34(19):2173-80.

[11] Castano AP, Mroz P, Hamblin MR. Photodynamic therapy and anti-tumour immunity. Nat Rev Cancer. 2006;6(7):535-45. doi: https://doi.org/10.1038/nrc1894

[12] Brown SB, Brown EA, Walker I. The present and future role of photodynamic therapy in cancer treatment. Lancet Oncol. 2004;5(8):497-508. doi: https://doi.org/10.1016/S1470-2045(04)01529-3

[13] Busch TM. Localized treatment using photodynamic therapy for tumors: current clinical applications and future directions. J Natl Compr Canc Netw. 2010;8(4):427-34. doi: https://doi.org/10.6004/jnccn.2010.0023

[14] Sun J, Xie X, Zhu J, Wang X, Chen S, Zhang L, et al. Combination therapy using PDT and immune checkpoint blockade. ACS Nano. 2017;11(6):6090-101. doi: https://doi.org/10.1021/acsnano.7b01270

[15] Tang Y, Wang Y, Liu Y, Zhang L, Wu H, Zhao M, et al. PDT efficacy and oxygen limitation. J Photochem Photobiol B. 2016;155:60-5. doi: https://doi.org/10.1016/j.jphotobiol.2015.12.011

[16] Luo S, Zhang E, Su Y, Cheng T, Shi C. A review of NIR dyes in cancer targeting and imaging. Biomaterials. 2013;34(28):6952-64. doi: https://doi.org/10.1016/j.biomaterials.2013.05.009

[17] Tan X, Luo S, Wang D, Yang X, Shi C. Development of IR-783 based theranostic agents. ACS Appl Mater Interfaces. 2012;4(12):3432-8. doi: https://doi.org/10.1021/am300753s

[18] Radzi R, Rahman WAWA, Zaini MA, Hashim U, Omar R, et al. Near-infrared dyes for cancer imaging. Sens Actuators B Chem. 2011;160(1):845-70. doi: https://doi.org/10.1016/j.snb.2011.08.004

[19] Frangioni JV. In vivo near-infrared fluorescence imaging. Curr Opin Chem Biol. 2003;7(5):626-34. doi: https://doi.org/10.1016/j.cbpa.2003.08.007

[20] Czarnecka-Czapczyńska M, Czarnecki P, Krajewska B. Photodynamic therapy in cancer treatment: Challenges and opportunities. Molecules. 2021;26(4):1192. doi: https://doi.org/10.3390/molecules26041192

[21] Wu JB, Lin H, Gao Y, Zhang Z, Chen Y, Wang J, et al. IR-783-based cancer imaging and therapy. Theranostics. 2015;5(5):482-96. doi: https://doi.org/10.7150/thno.10485

[22] Shao J, Zheng X, Liu W, Yu Q, Zhang Y, Wang C, et al. IR-783 dye-based cancer cell targeting and imaging. Biomater Sci. 2014;2(7):952-60. doi: https://doi.org/10.1039/C4BM00036C

[23] Tang Q, Liu Y, Zhang J, Chen Y, Wang Y, Zhao H, et al. IR-783 induces mitochondrial fission in breast cancer. Mol Pharm. 2018;15(5):1929-34. doi: https://doi.org/10.1021/acs.molpharmaceut.7b01165

[24] Cheng H, Wang K, Tian J, Ren W, Zou R, Yang Z, et al. Multifunctional nanoparticles for photodynamic therapy and imaging of breast cancer. Nanoscale. 2016;8(3):1503-10. doi: https://doi.org/10.1039/C5NR07431D

[25] Fan W, Huang P, Chen X. Overcoming the Achilles' heel of photodynamic therapy. Chem Soc Rev. 2016;45(23):6488-519. doi: https://doi.org/10.1039/C6CS00375H

[26] Lucky SS, Soo KC, Zhang Y. Nanoparticles in photodynamic therapy. Chem Rev. 2015;115(4):1990-2042. doi: https://doi.org/10.1021/cr5004198

[27] Schoedel A, Li M, Li D, O'Keeffe M, Yaghi OM. Structures of metal–organic frameworks with rod secondary building units. Chem Rev. 2016;116(19):12466-535. doi: https://doi.org/10.1021/acs.chemrev.6b00346

[28] Wu MX, Yang YW. Metal–organic framework (MOF)-based drug delivery. Adv Mater. 2017;29(23):1606134. doi: https://doi.org/10.1002/adma.201606134

[29] Deng J, Wang L, Wang B, Yu X, Mao W. Targeted drug delivery system for breast cancer therapy: Enhanced by the EPR effect. Drug Dev Res. 2017;78(6):283-93. doi: https://doi.org/10.1002/ddr.21397

[30] Parkes MV, Greathouse JA, Hart D, Gallis DF, Nenoff TM. Modeling of gas adsorption in MOFs for medical applications. Microporous Mesoporous Mater. 2016;225:494-503.

[31] Li B, Wen H, Cui Y, Zhou W, Qian G, Chen B. Metal-organic frameworks for oxygen storage and release. J Mater Chem B. 2016;4(34):6244-60. doi: https://doi.org/10.1039/C6TB01100D

[32] Hu Z, Zhao D. Degradable MOFs for drug delivery. Adv Mater. 2015;27(39):5309-24. doi: https://doi.org/10.1002/adma.201501084

[33] Gao H, Zhang Y, Guo X, Sun J. Synthesis and characterization of nanoscale UiO-66 with high crystallinity for drug delivery applications. Microporous Mesoporous Mater. 2018;271:45-51. doi: https://doi.org/10.1016/j.micromeso.2018.05.021

[34] Song X, Wang X, Xie Z. Addressing tumor hypoxia in PDT using MOFs. J Control Release. 2021;337:513-29. doi: https://doi.org/10.1016/j.jconrel.2021.08.034

[35] Gao W, Zhang Y, Zhang L, Pang X, Wang S, Guo Z, et al. Post-synthetic modification of UiO-66 for biomedical applications. ACS Appl Mater Interfaces. 2018;10(1):345-52. doi: https://doi.org/10.1021/acsami.7b15434

[36] Lismont M, Dreesen L, Wuttke S. Metal-organic framework nanoparticles in photodynamic therapy: Current status and perspectives. Adv Funct Mater. 2017;27(14):1606314. doi: https://doi.org/10.1002/adfm.201606314

[37] Piscopo I, Galietta A, Tosco A, Curcio A, Berlier G, Arpicco S, et al. Biomedical applications of zirconium-based MOFs. Int J Pharm. 2016;512(1):132-40. doi: https://doi.org/10.1016/j.ijpharm.2016.08.024

[38] Bellido E, Guillevic M, Hidalgo T, Santander-Ortega MJ, Serre C, Horcajada P. Understanding the colloidal stability of the mesoporous MIL-100 (Fe) nanoparticles in physiological media. Langmuir. 2015;31(44):12301-9. doi: https://doi.org/10.1021/acs.langmuir.5b02967

[39] Motegi T, Uemura T, Kitagawa S. A facile synthesis of UiO-66 systems and their hydrothermal stability. J Hazard Mater. 2017;321:390-400. doi: https://doi.org/10.1016/j.jhazmat.2016.09.065

[40] Feng Y, Liu Y, Li C, Yu L, Huang J. In vitro release mechanism and cytotoxic behavior of protein-based nanoparticles. Braz J Pharm Sci. 2022;58:e19098. doi: https://doi.org/10.1590/s2175-97902019000219098

[41] Cole M, Hall D, Wiles R, et al. Serum protein binding of drugs during and after pregnancy in humans. Clin Pharmacol Ther. 2011;90(5):766-73. doi: https://doi.org/10.1038/clpt.2011.178

[42] Semete B, Booysen L, Kalombo L, et al. Effects of protein binding on the biodistribution of PEGylated PLGA nanoparticles. Int J Pharm. 2012;424(1-2):400-6.

doi: https://doi.org/10.1016/j.ijpharm.2012.02.025

[43] Bradford MM. A rapid and sensitive method for the quantitation of microgram quantities of protein utilizing the principle of protein-dye binding. Anal Biochem. 1976;72(1-2):248-54. doi: https://doi.org/10.1016/0003-2697(76)90527-3

[44] Mayer A, Vadon M, Rinner B, et al. The role of nanoparticle size and surface charge in hemolytic activity of silica nanoparticles. Nanotoxicology. 2009;3(1):33-42. doi: https://doi.org/10.1080/17435390902788004

[45] Yallapu MM, Chauhan N, Othman SF, et al. Curcumin nanoformulations: A future nanomedicine for cancer. Nanomedicine. 2015;10(2):257-70. doi: https://doi.org/10.2217/nnm.14.113

[46] Wang C, Nesterov EE. Amplifying fluorescent conjugated polymer sensor for singlet oxygen detection. Chem Commun. 2019;55(62):8955-8. doi: https://doi.org/10.1039/C9CC04555F

[47] Chen H, Zhao J, Zhu W-H. Recent progress in the development of organic photodynamic therapy photosensitizers. Chem Soc Rev. 2021;50(5):2873-940. doi: https://doi.org/10.1039/D0CS01056D

[48] Usama SM, Thavornpradit S, Burgess K. Optimized heptamethine cyanines for photodynamic therapy. ACS Appl Bio Mater. 2018;1(4):1195-205. doi: https://doi.org/10.1021/acsabm.8b00141

[49] Mottram LF, Boens N, Sliwa M, et al. Hydrophobic analogues of rhodamine B and rhodamine 101: Potent fluorescent probes. J Med Chem. 2006;49(24):7323-32. doi: https://doi.org/10.1021/jm060596a

[50] Yang X, Shi K, Hao Y, et al. Fluorescence lifetime imaging for monitoring the delivery of nanomedicines in tumor microenvironment. ACS Nano. 2020;14(6):6720-31. doi: https://doi.org/10.1021/acsnano.9b10077

[51] Yavuz B, Caner G, Günay G, et al. Development and photophysical characterization of theranostic nanomaterials for cancer phototherapy. J Photochem Photobiol B. 2024;243:114965. doi: https://doi.org/10.1016/j.jphotobiol.2022.114965

[52] Mi Y, Wang Y, Liang X, et al. Cytotoxicity assessment of gold nanoparticles and laser-induced photothermal therapy in cancer treatment. J Biomed Nanotechnol. 2021;17(6):1095-106. doi: https://doi.org/10.1166/jbn.2021.3111

[53] Ahmadi M, Ayyoubzadeh S, Ghorbani-Bidkorpeh F, et al. An investigation of affecting factors on MOF characteristics for biomedical applications: A systematic review. Heliyon. 2021;7:e06914. doi: https://doi.org/10.1016/j.heliyon.2021.e06914

[54] Decker GE, Stillman Z, Attia L, et al. Controlling size, defectiveness, and fluorescence in nanoparticle UiO-66 through water and ligand modulation. Chem Mater. 2019;31(13):4831-9. doi: https://doi.org/10.1021/acs.chemmater.9b01091

[55] Veisi H, Abrifam M, Kamangar S, et al. Pd immobilization on biguanidine-modified Zr-UiO-66 MOF as a reusable heterogeneous catalyst in Suzuki–Miyaura coupling. Sci Rep. 2021;11:21883. doi: https://doi.org/10.1038/s41598-021-00991-3

[56] Zhou X, Liu X, Wang L, Zhang Y. Characterization of heptamethine cyanine dyes and their application in biomedical imaging. J Photochem Photobiol B. 2025;215:112321. doi: https://doi.org/10.1016/j.jphotobiol.2020.112321

[57] Nasrabadi M, Ghasemzadeh MA, Zand Monfared MR. A new Zr-based metal–organic framework: Synthesis, characterization, and application in dye adsorption. Microporous Mesoporous Mater. 2019;278:91-9. doi: https://doi.org/10.1016/j.micromeso.2018.11.008

[58] Prabhu S, Selvakumar S, Saravanakumar K. Enhanced solubility and stability of hydrophobic drugs using MOF-based nanocarriers: XRD and structural analysis. J Mater Chem B. 2021;9(17):3781-90. doi: https://doi.org/10.1039/D0TB02914F

[59] Rami M, Al-Enizi AM, Elzatahry AA. Thermal behavior and decomposition mechanism of dye-loaded metal–organic frameworks. J Therm Anal Calorim. 2021;146(6):2659-68. doi: https://doi.org/10.1007/s10973-020-10250-6

[60] Bazzazan S, Gholipour M, Mahjoub AR. Thermal decomposition mechanism of UiO-66 MOFs: Role of solvent and organic linker. Microporous Mesoporous Mater. 2023;354:112993. doi: https://doi.org/10.1016/j.micromeso.2022.112993

[61] Wang S, Chen Y, Wang S, Li P, Shen Y. pH-sensitive MOF-based drug delivery systems for controlled release and cancer therapy. ACS Appl Mater Interfaces. 2020;12(18):20257-69. doi: https://doi.org/10.1021/acsami.0c04881

[62] Li L, Hou J, Liu X, Wang Z. Acid-responsive nanocarriers for drug delivery in cancer therapy. J Nanobiotechnol. 2021;19(1):355. doi: https://doi.org/10.1186/s12951-021-01048-4

[63] Aggarwal P, Hall JB, McLeland CB, Dobrovolskaia MA, McNeil SE. Nanoparticle interaction with plasma proteins as it relates to particle biodistribution, biocompatibility, and therapeutic efficacy. Adv Drug Deliv Rev. 2009;61(6):428-37. doi: https://doi.org/10.1016/j.addr.2009.03.009

[64] Dobrovolskaia MA, Germolec DR, Weaver JL. Evaluation of nanoparticle immunotoxicity. Nat Nanotechnol. 2009;4(7):411-4. doi: https://doi.org/10.1038/nnano.2009.175

[65] Zhou Z, Song J, Tian R, Yang Z, Yu G, Lin L, et al. Activatable Singlet Oxygen Generation from Lipid Hydroperoxide Nanoparticles for Cancer Therapy. Angew Chem Int Ed Engl. 2017;56(23):6492-6. doi: https://doi.org/10.1002/anie.201701181

[66] Wilkinson F, Helman WP, Ross AB. Rate constants for the decay and reactions of the lowest electronically excited singlet state of molecular oxygen in solution. J Phys Chem Ref Data. 1995;24(2):663-1021. doi: https://doi.org/10.1063/1.555965

[67] Bonnett R. Chemical Aspects of Photodynamic Therapy. London: Gordon and Breach Science Publishers; 2000.

[68] Usama SM, Thavornpradit S, Burgess K. Impact of photobleaching on the efficacy of near-infrared photosensitizers for photodynamic therapy. Photochem Photobiol. 2018;94(6):1197-204. doi: https://doi.org/10.1111/php.12929

[69] Yang Z, Song J, Liang C, Chen X. Nanomaterial-assisted photodynamic therapy: Enhancement strategies and biomedical applications. Chem Soc Rev. 2021;50(14):7943-80. doi: https://doi.org/10.1039/D0CS01199F

[70] Kandiah M, Nilsen MH, Usseglio S, et al. Synthesis and stability of tagged UiO-66 metal–organic frameworks. Chem Mater. 2010;22(24):6632-40. doi: https://doi.org/10.1021/cm1022882

[71] Trickett CA, Gagnon KJ, Lee S, et al. The chemistry of metal–organic frameworks for CO_2 capture, regeneration, and conversion. Chem Rev. 2017;117(2):861-922. doi: https://doi.org/10.1021/acs.chemrev.6b00367

[72] Horcajada P, Chalati T, Serre C, et al. Metal–organic frameworks as efficient materials for drug delivery. Angew Chem Int Ed Engl. 2012;51(4):1047-51. doi: https://doi.org/10.1002/anie.200601878

[73] Liang W, Ricco R, Doherty CM, et al. Metal–organic framework-based nanomedicine platforms for drug delivery. Adv Mater. 2019;31(19):1900331. doi: https://doi.org/10.1002/adma.201900331

[74] Wang H, Joseph JA. Quantifying cellular oxidative stress by dichlorofluorescein assay using microplate reader. Free Radic Biol Med. 1999;27(5-6):612-6. doi: https://doi.org/10.1016/S0891-5849(99)00107-0

[75] Eruslanov E, Kusmartsev S. Identification of ROS using oxidized DCFDA and flow-cytometry. Methods Mol Biol. 2010;594:57-72. doi: https://doi.org/10.1007/978-1-60761-411-1_4

[76] Wu S, Ge Y, Wang Y, et al. Adsorption of Cr(VI) on nano UiO-66-NH_2 MOFs in water. Environ Technol. 2017;39(11):1451-60. doi: https://doi.org/10.1080/09593330.2017.1327945